

We are IntechOpen, the world's leading publisher of Open Access books Built by scientists, for scientists

6,900

Open access books available

185,000

International authors and editors

200M

Downloads

Our authors are among the

154

Countries delivered to

TOP 1%

most cited scientists

12.2%

Contributors from top 500 universities



WEB OF SCIENCE™

Selection of our books indexed in the Book Citation Index
in Web of Science™ Core Collection (BKCI)

Interested in publishing with us?
Contact book.department@intechopen.com

Numbers displayed above are based on latest data collected.
For more information visit www.intechopen.com



Miniaturized Gas Ionization Sensor Based on Field Enhancement Properties of Silicon Nanostructures

Parsoua Abedini Sohi and Mojtaba Kahrizi

Abstract

According to principle of the operation, gas field ionization sensors are classified as transduction-based gas sensors. These sensors identify the unknown gases based on their unique ionization properties such as breakdown voltage or tunneling current. Applying 1D nanostructure in gas ionization sensors would enhance the local electric field at the tip of the structures. The average field enhancement coefficient (β_{tol}), considering constructive/destructive interferences of the local electric field of thousands of nanowires in the whole structure, is desired to optimize the design and structure of the gas sensors. Using chemical/electrochemical techniques silicon nanowires were grown on one of the electrodes of the gas sensor. Mechanism of the nanowires formation was modeled and simulated using COMSOL multiphysics simulation tool prior to their fabrication. A gas field ionization tunneling sensor, was designed, fabricated, and tested successfully for several gases like N_2 , He, and Ar. Estimated β_{tol} of the sensor showed that the electric field strength inside the sensor is 3750 times greater than a planar parallel-plate sensor causing to reduce the breakdown voltages from several thousand volts to the range of 60–70 V for various gases.

Keywords: gas ionization sensor, tunneling current, field enhancement factor, COMSOL, silicon nanowires

1. Introduction

There are several natural and artificial chemical species in the air, some of which are toxic and combustible gases, which can be considered as potential hazard to the health [1–3]. Gas sensors helps to prevent these hazards and play an important role in places with the risk of potentially harmful substances specifically in industrial processes and manufacturing plants.

Depending on the principal of the operation, gas sensor devices can be classified into two distinct categories: chemical gas sensors and physical gas sensors [3]. Merely, considering transduction mechanism, chemical gas sensors are based on chemical reaction between gas and sensing materials, resulting in change of conductivity of the detector material. In this method, gases in different combinations could produce the same net-change in conductance and as a result, distinguishing between a gas and its mixtures is impossible. These types of sensors are very

sensitive to changes in moisture, temperature and gas pressure. Their other drawback is that chemical reactions could cause irreversible changes in detector materials [3]. Physical type sensors have overcome the disadvantages of chemical type sensors. There are several physical type gas sensors, according to the mechanism of operation, including surface plasmon resonance (SPR) based [4] gas sensors, fiber optic based gas sensors [5–8] and gas ionization sensors [9].

Surface plasmon resonance (SPR) is the resonant oscillations of surface electrons, which are stimulated by incident illumination at the interface between a metal and dielectric [10, 11]. SPR is very sensitive to the refractive index of the medium close to the metal film. The resonance spectral response of the SPR will change when the conditions of the medium are changed, which can reflect certain properties of the system. Kretschmann geometry (prism coupler) is widely used to study SPR. In this configuration, optical wave is totally reflected at prism-metal interface [12]. Evanescent field wave may penetrate the metal layer and excite surface plasmon at the metal-dielectric boundary. As excitation of surface plasmon significantly reduces the intensity of reflected light, reflectivity of the sensor as a function of either wavelength or incident angle is considered as the sensor response [12].

Agbor et al. [13] reported the SPR gas sensing measurements in Kretschmann configuration using nickel/silver coated glass microscope slides. According to their results, the SPR curves were influenced by 50 ppm of NO_2 and H_2S at room temperature. Maharana et al. [14] reported a numerical study on a high performance SPR sensor based on graphene coated silver on wide range of refractive indices of gases. Graphene is widely used in SPR based gaseous detection systems, as its refractive index is highly sensitive to the absorbed gas molecules. Furthermore, graphene is robust against the oxidation and the layer of graphene in SPR sensors (in presence of noble metals) prevents oxidation of the silver layer. Nooke et al. [15] studied the SPR gas sensing measurements in Kretschmann configuration using gold (Au) coated glass for combustible, toxic and greenhouse gases. They also reported that the gas detection limit is related to the rate of gas adsorption, which is defined by polarizability of the gases.

SPR-based fiber optic sensors are designed by replacing the cladding with a thin layer (in nm range) of metal. In these sensors it is hard to reach the sensitivity similar to Kretschmann SPR configuration due to complexity in controlling the incidence angle of light, impossibility to control the wave polarization and an excessive number of reflections. In these sensors the spatial-frequency bandwidth of their angular spectrum is wider in comparison with other types of SPR sensors [16, 17]. However, some noticeable advantages like low cost, flexibility, real-time monitoring, compatibility with human tissue and blood vessels, remote sensing, small sample volume, reusability, and simple structure have made the SPR fiber optic approach very attractive.

Gas sensing application of the fiber optic sensor was developed in 1980 [1] and the sensing measurements are essentially based on changing the features of transmitted light along the fiber. Transmitted light can be modified in response to external medium properties. According to the principal of the operation, fiber optic gas sensor devices can be classified into two distinct categories: extrinsic and intrinsic [1, 6]. In extrinsic fiber optic gas sensors, light exits the fiber and interacts with the medium before continuing propagation inside the core again. In these sensors, light propagates through the input fiber optic toward a microcell containing the unknown gas. The output signal is guided to a spectrometer using the output fiber optic, which is accurately aligned with the input one. This provides the unknown gas detection by comparing the input interrogating wavelength and the absorption spectrum of the gas [6]. This technique can be only used for the gases which spectral absorption is in the range of telecommunication window so the fiber can be successfully employed. Stewart et al. [18] reported a design of fiber optic methane sensor using a microcell and DFB laser source. The theoretical modeling of the designed

sensor was in a good agreement with experimental results and both showed a single absorption line for the methane gas.

Shemshad et al. [19, 20] investigated the absorption band of methane and stated that absorbance spectrum of methane is between 1620 and 1700 nm which is suitable for fiber optic detection sensors. As methane is released during coal extractions, they have also studied the cross sensitivity of methane with other gases emitted from mine. Their results showed that the absorbance spectrum of methane does not interfere with other gases in the mine.

In intrinsic fiber optic gas sensors, light propagates inside the core continuously without any external interaction. When a light is propagating through fiber optics, at the core-cladding boundary it undergoes total internal reflection (TIR). During each TIR it penetrates into the cladding region, which is known as evanescent wave. The amplitude of the evanescent wave decays exponentially in the cladding region. So the cladding (with lower refractive index) absorbs a small portion of propagating light energy. This process is known as attenuated total reflection (ATR). If an absorbing chemical or testing sample is present with the evanescent field region, the propagating light will be attenuated (as the reflection coefficient is less than unity) as it travels along the fiber. Since the energy levels associated with an atom or molecules are unique, the absorption spectrum serves as a “fingerprint” identification of the chemical species [1]. To increase the sensitivity of such sensors the cladding can be manufactured to be sensitive to specific organic vapors [21] or an unclad fiber can be coated with sensitive coatings [22]. Another alternative way is diminishing the cladding thickness, which results in a more fragile but more sensitive sensor [6, 20].

Gas field ionization sensors identify unknown gases by their unique ionization characteristics [23]. Calibration of these devices is based on fingerprinting breakdown voltage of the target gases. The gas sensor is made of two parallel planar electrodes. The two plates are separated by pieces of insulating films such a way that there is enough opening between the two electrodes to allow the gas flow between them. Applied voltage across the device is swept and insulation-to-conduction transformation of the gas (known as breakdown), using I-V characteristics of electrical discharge, is recorded [23]. This technique has improved selectivity property of the gas sensors, as it is approved that at a constant pressure and temperature, each gas has unique breakdown voltage (or breakdown electric field) [9]. An applied voltage required to generate breakdown electric field (E_{app}), depends on the separation gap between the plates and typically is over several hundred volts [24–26]. As applying this voltage is not practical, to scale down the breakdown voltage of the gases, 1D nanostructures could be applied as one of the electrodes. Enhanced local electric field (E_{loc}) is created at the tip of the nanostructures due to non-uniform distribution of charged carriers [27, 28]. Field enhancement factor (β) characterizes the level of influence of the 1D nanostructures onto the electrostatic field distribution and can be defined as the field gain coefficient ($\beta = E_{loc}/E_{app}$) [27].

In this work we have explored an example of gas ionization sensor that is fabricated based on p-type silicon (Si) nanostructures. The ionization characteristics of several gases are reported. The effect of applying these structures on the field enhancement factor of the sensor, compared to a parallel plate system, is described.

2. Geometrical field enhancement

Nanowires amplify E_{loc} regardless of their bias direction. However depending on the type of the materials of the nanowires some promote field emission, and others will enhance field ionization tunneling phenomenon.

In field emission based gas sensors, Fowler Nordheim (FN) theory of electron emission from a metallic or semi-metallic roughly predicts β_{tol} based on the field induced emission current and can be experimentally calculated by plotting $\ln(J/V^2)$ against $(1/V)$ where J is the emission current density and V is the applied voltage [41, 42].

In the second approach, this factor can be estimated practically using the slope of the gas discharge graph (I-V characteristics) in the ohmic region of the curves (for field emission gas sensors as well as field ionization tunneling sensors). **Figure 2** shows different regions of discharge characteristic of gases in a uniform electric field generated between planer parallel plates. Any gas contains free-floating negative electrons and positive ions due to the ionization of the gas atoms by cosmic radiation. In region I of the discharge curve, when the voltage is applied to the electrodes, the traveling radiation-generated charged particles produce current as electrons migrate to the anode and the ions move toward the cathode. The current in this region shows strong electric field dependence and increases as the applied voltage is increased. In this region the discharge current density is expressed as:

$$J_{GIS} = \sigma_{Gas} \times E_{app} = (n_e \mu_e + n_i \mu_i) \times e \times E_{app} \quad (1)$$

where σ_{Gas} is the gas conductivity, e the electron charge, E_{app} the applied electric field, n_e and n_i the electron and ion concentrations respectively, and μ_e , and μ_i are the electron and ion mobility respectively.

In saturation region (II), the current reaches its saturated value which means that all radiation-generated particles are attracting to the electrodes. At the last phase the electric field strength would be enough to accelerate the electrons, resulting ionizing collisions. At breakdown voltage (V_b) the discharge current is self-sustainable and is maintained due to ionizing collisions without any external ionization source.

According to Eq. (1) in the ohmic region, the traveling radiation-generated charged particles produce current proportional to applied field. As in this region there is no ionization-induced current, the current density exclusively depends on the strength of the electric field. The current density of nanowire based gas ionization sensor (J_{GIS}) due to enhanced electric field can be expressed as

$$J_{GIS} = \sigma_{Gas} \times E_{eff} = (n_e \mu_e + n_i \mu_i) \times e \times \beta_{tol} \times E_{app} \quad (2)$$

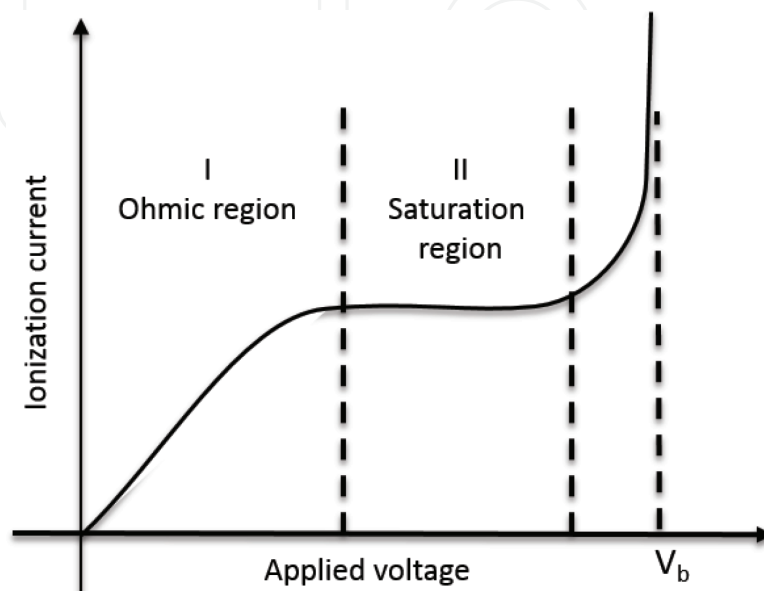


Figure 2.
 I-V characteristics of gas discharge in a uniform electric field.

where E_{eff} is the enhanced electric field and β_{tol} is average field gain coefficient.

By comparing Eqs. (1) and (2) and considering a constant σ_{Gas} , β_{tol} of gas ionization sensors can be estimated by dividing the slopes of I-V characteristics of the device with a parallel-plates in the ohmic region.

$$\beta_{tol} = \frac{Slope_{GIS}}{Slope_{PPL}} \quad (3)$$

where $Slope_{GIS}$ is the slope of I-V discharge graph of the nanowire based GIS and $Slope_{PPL}$ is the slope of the I-V discharge graph of the parallel plate in their ohmic regions.

3. Fabrication of silicon nanostructures

Silicon nanostructures are fabricated using chemical/electrochemical technique [43]. Samples of p-type <100> silicon wafers ($380 \pm 10 \mu\text{m}$ thickness with resistivity about $5\text{--}10 \Omega \text{ cm}$ from Silicon Material Inc.) were cut in $1 \times 1 \text{ cm}^2$ pieces and cleaned using RCA technique. In the first step of etching, samples were textured by pyramidal structures through anisotropic etching in tetramethylammonium hydroxide (TMAH) based solution. The solution for anisotropic etching, made of equal amount of TMAH and isopropyl alcohol (IPA) (5 wt% each), was used to etch the samples for 20 minutes. The temperature of the solution was kept constant at 90°C using an oil bath system. A condenser covered the etchant container in order

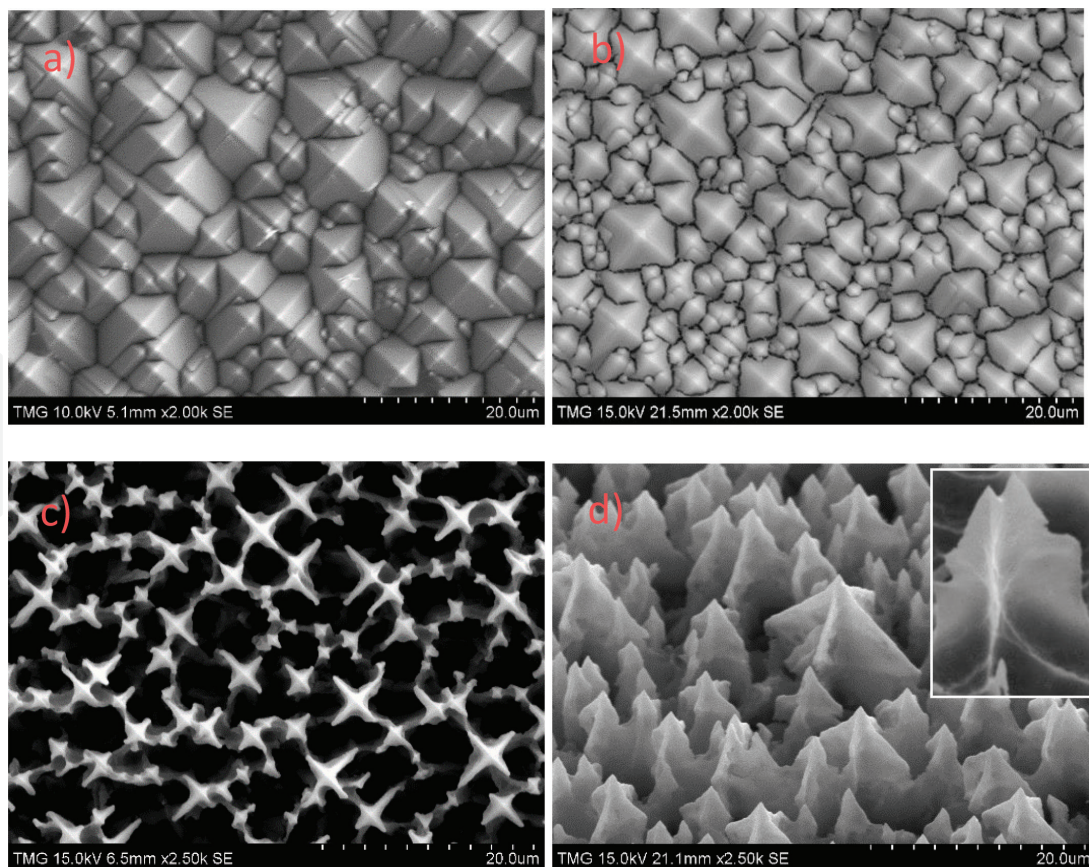


Figure 3.

Experimental results of the evolution of the nanostructures. (a) Anisotropic etching of <100> p-type silicon at 90°C for 20 minutes in 5 wt% TMAH and 5 wt% IPA resulted in formation of pyramids that covers the surface completely. (b) Top view of the electrochemically etched textured silicon after 10 minutes of etching. (c) Top view of the electrochemically etched silicon after 70 minutes. (d) Top view of the electrochemically etched silicon after 70 minutes. (d-inset) Tilted view of the final nanostructures illustrates the existence of residual walls around the structures with the thickness of 100 nm.

to keep the etchant concentration constant throughout the experiment. **Figure 3a** shows the SEM image of textured Si sample containing square-based pyramidal structures after anisotropic etching step. As it is shown in the figure, the average tip-to-tip separation of the large pyramids is more than 5 μm . The samples were subsequently exposed to electrochemical isotropic etching. In this step the textured silicon samples, are placed in a two-electrode cell of anodic etching. The etching was done in an electrolyte consisting of 1:3 hydrofluoric acid and ethanol for 70 minutes under a 15 mA/cm^2 applied anodic current density. Porous silicon starts to form by electrochemical etching, all around the pyramids. **Figure 3b** shows the SEM image of electrochemically etched sample after 10 minutes of etching. As the etching continues, the pyramid faces are etched away, while lateral edges remain unetched. **Figure 3c** and **d** shows the top view and tilted view SEM image of the sample after 70 minutes isotropic etching. To narrow down the lateral edges, samples are subjected to another anisotropic etching in a weak etchant solution (1 wt% of TMAH and 1 wt% of IPA) for 30 seconds. The final structures are shown in the inset of **Figure 3d**. They are arrow shape structures with remaining lateral edges with the thickness about 100 nm.

4. Formation mechanism of the nanostructures

Electrochemical dissolution of Si, in the second step of etching, is highly influenced by hole current density at the interface of Si/electrolyte. Hole drift current density in semiconductors can be found by,

$$J_p = e \times p \times \mu_p \times E \left(\frac{\text{A}}{\text{cm}^2} \right) \quad (4)$$

Where e is electric charge (1.6×10^{-19} coulomb), p is the concentration of holes/ cm^3 , μ_p is the hole mobility ($\text{cm}^2/\text{V s}$) and E is the applied electric field (V/cm).

Eq. 4 confirms the dependence of the etching rate with the electric field strength. According to **Figure 3b** the pyramid perimeters are experiencing a higher etching rate at the beginning of the etching process. This can be attributed to maximum electric field intensity at those regions.

Due to uneven textured Si surfaces, the electric field is not uniform at the interface. As a result, the hole drift current density is not uniform over the surface of the samples and different areas are experiencing different dissolution rates during the anodic etching.

The electric field intensity generated at textured Si (anode) is modeled and simulated utilizing COMSOL, electrostatics module. To study the evolution mechanism we have considered the 3D schematic geometry and initial electric field distribution shown in **Figure 4** when voltage is applied to the backside of the textured Si. Simulation results shows that the electric field is not uniform and the lowest belongs to tips and lateral edges of the pyramids, and highest is for pyramid perimeters.

To present the development of the structures, COMSOL deformed geometry (dg) physics interface is applied to all domains. A prescribed mesh velocity is assigned to the boundary between Si and electrolyte (pyramidal texture) and a prescribed mesh displacement is assigned to boundaries all around the block. Moving mesh velocity is defined proportional to electric field.

Figure 5 clearly shows that the etching and developing porous silicon start at the edges of the pyramids bases where the electric field has the maximum value.

As the etching extends, pyramid faces are etched away while lateral edges remain as connecting walls between the pyramids. **Figure 6** clearly illustrates the residual walls between the structures.

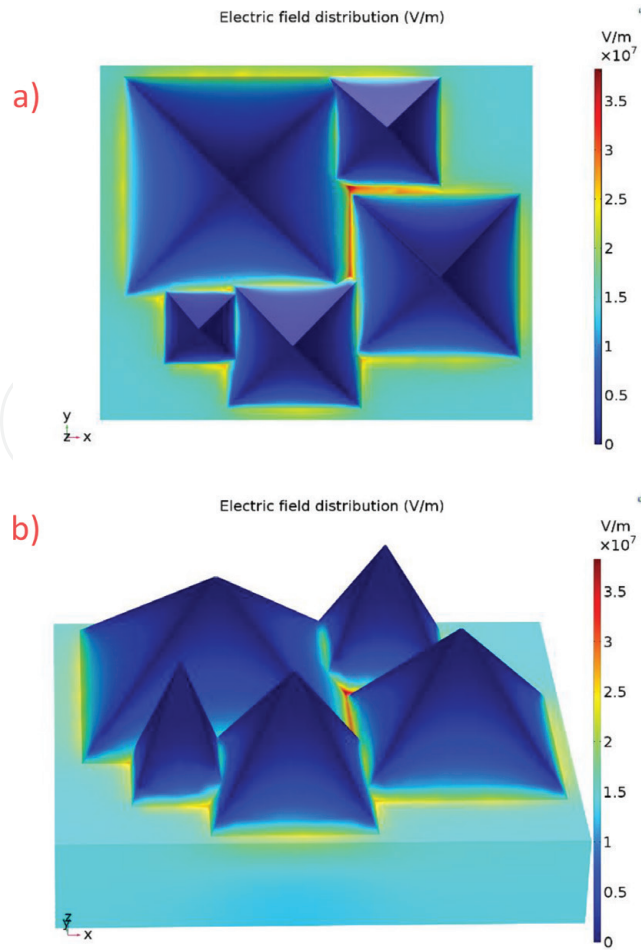


Figure 4. Distribution of electric field in the textured Si surface is simulated by COMSOL electrostatics module. (a) Top view and (b) tilted view of the 3D structures shows that the electric field strength is not uniform and the lowest belongs to vertex and sides (shown by dark blue) and highest is for pyramid perimeters (shown in yellow/red).

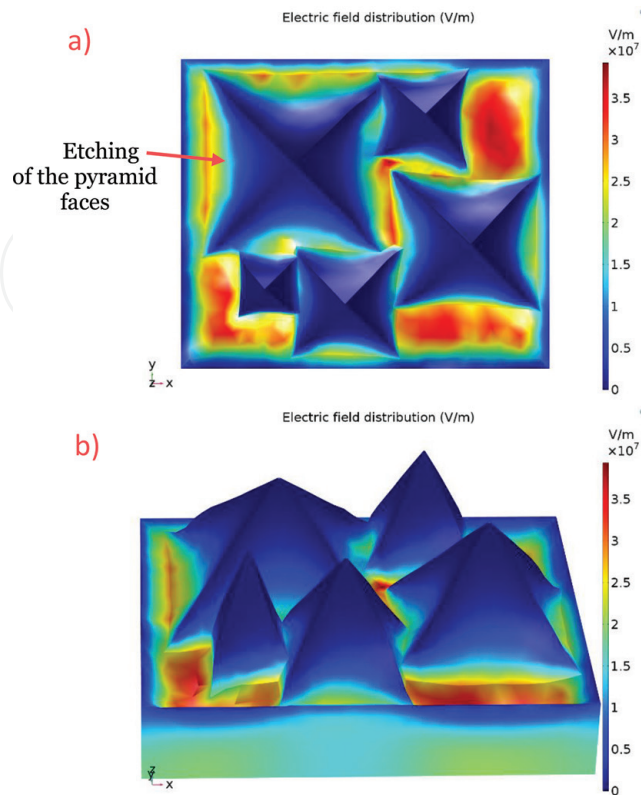


Figure 5. (a) Top view and (b) tilted view of COMSOL deformed geometry. The figures show that as the etching starts, pyramid perimeters are experiencing higher etching rates due to higher electric field strength.

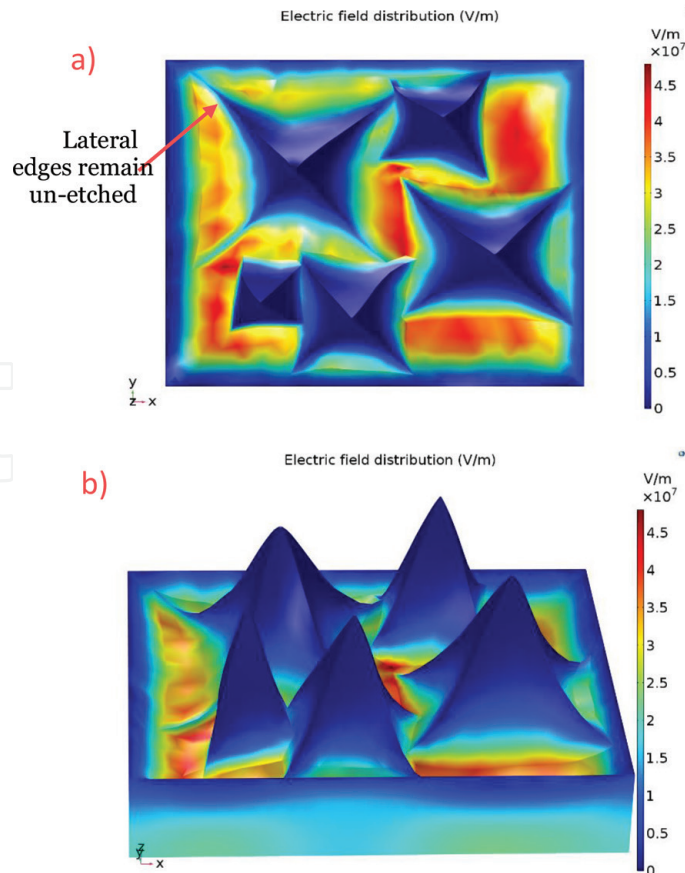


Figure 6. COMSOL deformed geometry shows that the extended etching results in residual walls around the structures, while pyramid faces are etched away. (a) Top view, (b) tilted view.

5. Device fabrication and sensor setup

Fabricated Si nanostructures were incorporated as the anode in gas ionization cell. The cathode is a piece of p-type Si cleaned with RCA method and coated with a 5 μm aluminum (Al) layer using thermal evaporation technique. The electrodes are separated, using an insulating thin film (double sided adhesive tape), by a narrow gap but wide enough to allow the flow of the gases through the cell. **Figure 7** shows the schematic illustration of the gas ionization cell.

The device was placed in the gas chamber and vacuumed to 10^{-5} Torr prior to introduce each gas to the chamber. The electrodes are connected to two source measure units (SMUs) of a HP4155 semiconductor parameter analyzer and I-V characteristics of the device was conducted by sweeping the voltage of the anode

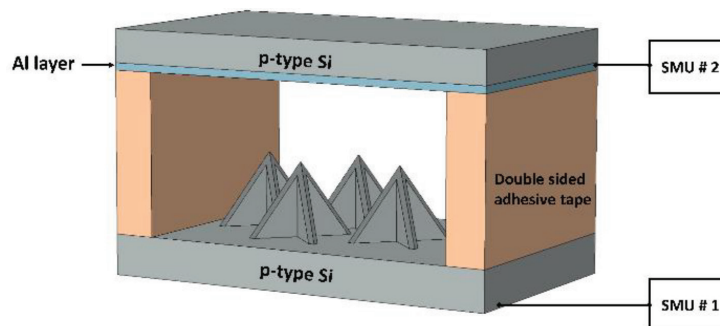


Figure 7. Schematic of Si nanowires-based GITS. Fabricated sample is applied as the anode and it attached to SMU #1 of the parameter analyzer. An Al coated Si is applied as the cathode. Electrodes are separated by two pieces of double sided adhesive tape. The other sides are left open to facilitate the gas flow through the sensor.

from 0 to 100 V, with steps of 1 V and 1 second sweep delay. The sensor was tested for oxygen (O₂), argon (Ar), Nitrogen (N₂) and helium (He) at low pressures.

6. Results and discussions

6.1 Estimation of β_{tot}

To calculate the total field gain coefficient (β_{tot}) based on Eq. (3), I-V characteristics of a PPL sensor is compared to that of the GITS. The parallel-plates sensor consists of two plates, one perfectly smooth p-type Si wafer as the anode and an aluminum coated Si wafer as the cathode, separated by 100 μm gap. GITS sensor is fabricated as explained in Section 5 with the same separation gap of 100 μm between the electrodes.

Ohmic regions of both PPL sensor and fabricated GITS, under vacuumed air (10^{-5} Torr), are shown in **Figure 8**. The total enhancement factor of the device is calculated using Eq. 3. Accordingly, the enhancement factor of the device is equal to:

$$\beta_{tot} = \frac{\text{Slope}_{GIS}}{\text{Slope}_{PPL}} \approx \frac{3 \times 10^{-5}}{8 \times 10^{-9}} = 3,750 \quad (5)$$

Theoretically, no tunneling occurs at electric fields less than 10^9 V/m. The electric field strength in the parallel plate sensor is in the range of 10^5 – 10^6 V/m according to applied voltage (100 V is the maximum voltage of HP4155-SMU). This value should at least increase by 1000 times to make the tunneling possible. Our estimated value of β_{tot} , indicates that the geometrical field enhancement of fabricated GITS induces the required electric field for the field ionization tunneling.

6.2 Characterization of the gas sensor

Field ionization tunneling tests were performed at 10^{-2} Torr for several gases, while separation gap between the electrodes was set at 200 μm . A 20 mA current compliance is applied to both SMUs in order to protect nanowires from burning.

Figure 9 shows the same trend for I-V characteristics of all the gases. Below 20 V the gas discharge is in its ohmic region, in which current is low and is due to the movement of radiation-generated charged particles. At the voltages above the ohmic region, contrary to ionization discharge curve of a PPL sensor (shown in

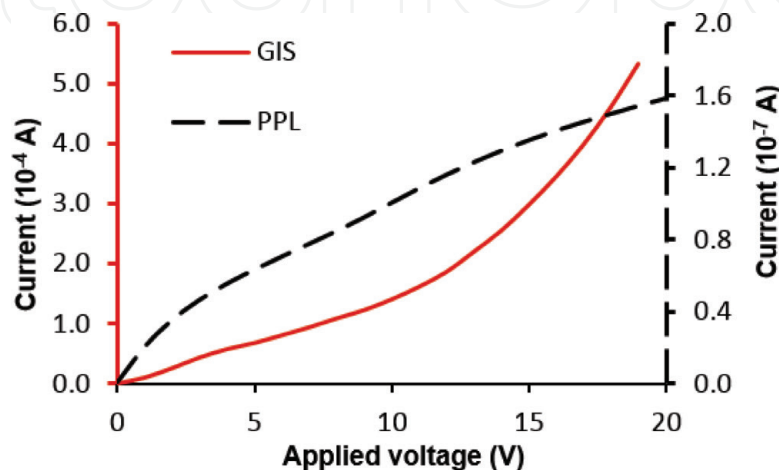


Figure 8. Ohmic regions of the PPL sensor and the fabricated GITS at 10^{-5} Torr vacuumed air. The slopes of the curves are used to calculate the enhancement factor of the system.

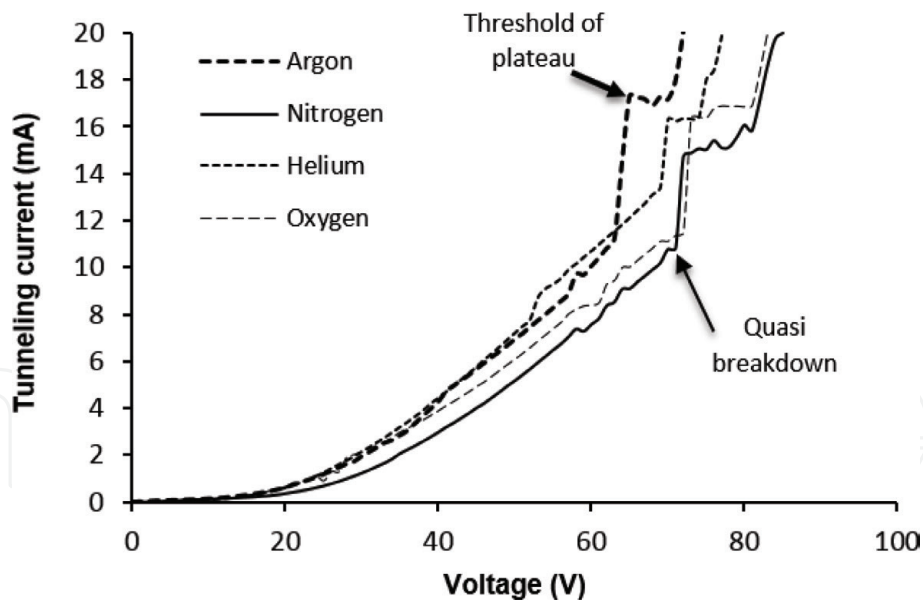


Figure 9. Room temperature I-V characteristics of Ar, N₂, He and O₂ at 10⁻² Torr show distinctive tunneling properties of the gases. The transition from ohmic region to tunneling region can be seen at 20 V, where the tunneling current increased steeply (reproduced from Abedini Sohi & Kahrizi [38]).

Figure 2) which reaches to a saturated current, the discharge current of fabricated GITS increases sharply as the applied voltage is increased. In this region the electric field is higher than ionization threshold and the valence electrons of the gases are able to tunnel through the potential barrier of the gas atom, into the unoccupied energy states of the anode electrode.

Each gas reaches to a quasi-breakdown (V_{qbr}) at a specific voltage. At V_{qbr} , an abrupt rise in the tunneling current is due to the cathode bombardment by positive ions, which results in gas amplification due to secondary emissions of the Al layer. Large number of positive ions is generated during the gas amplification and move toward the cathode to get neutralized. These positive ions create an internal electric field in opposite direction to the applied electric field. Consequently the total electric field is reduced, which reduces the rate of ionization and as a result the tunneling current reaches a plateau. After neutralization of the accumulated positive ions, the tunneling current is increased again until reaching current compliance.

The V_{qbr} and threshold of plateau can be used as calibrating data to distinguish the gases.

Figure 10 represents the room temperature I-V characteristics of the fabricated GITS for He (**Figure 10a**) and Ar (**Figure 10b**) at different pressures. According to the results, no correlation between the tunneling current and pressure can be addressed. However, the V_{qbr} for the both gases is raised as the pressure is increased. This increase in V_{qbr} can be explained by reduced mean free path (the average distance traveled by a particle to make successive ionizing collisions). As the mean free path is reduced in higher pressures, the electrons acquire enough energy to create impact ionizations at higher electric fields.

The experiments are extended to test the effect of separation gap between the electrodes on I-V characteristics of the sensor. For this reason, the same device with 50, 100 and 200 μm separation gaps was tested for Ar at 10⁻² Torr. As it is shown in **Figure 11**, by reducing the separation gap to 50 μm , the sensor showed a complete breakdown at 50 V due to the high electric field strength. At 100 μm a complete breakdown was observed at 60 V. Lower electric field in the devices with 200 μm separation gap, resulted in quasi breakdown and a threshold of plateau that is explained earlier.

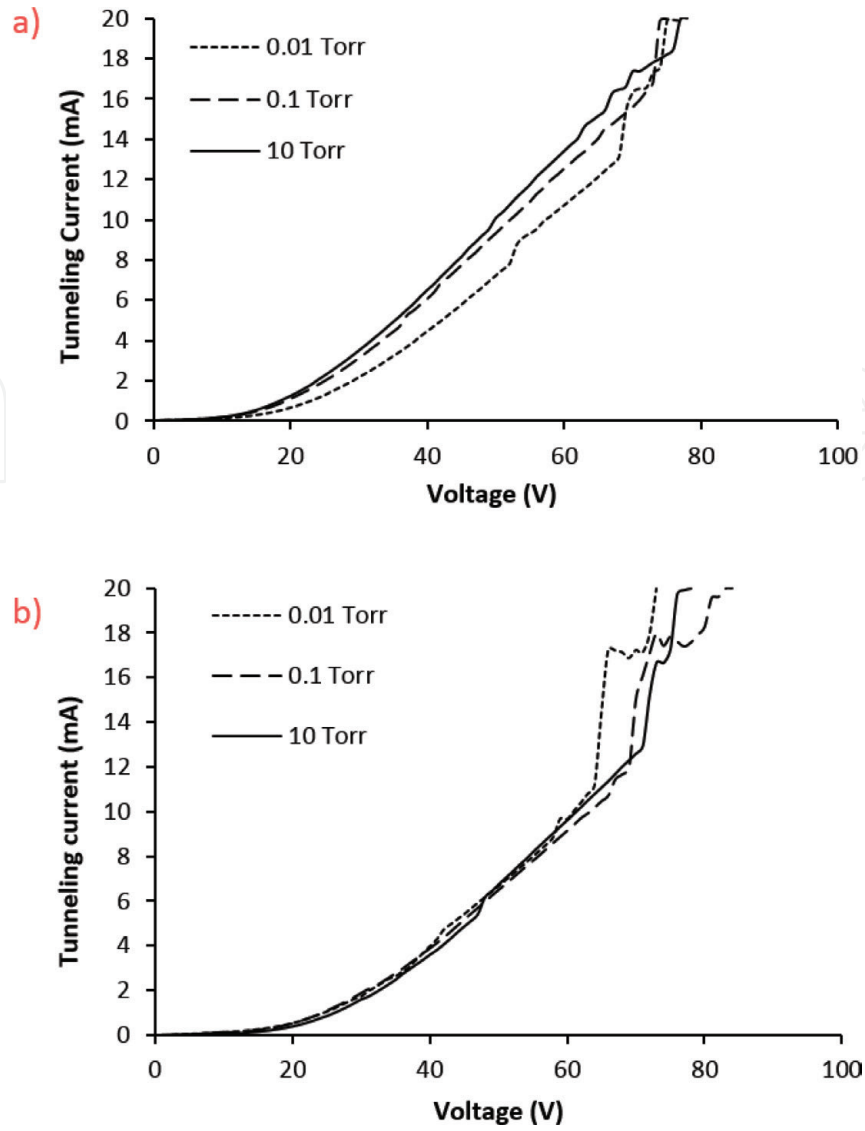


Figure 10. Room temperature $I-V$ characteristics of He (a) and Ar (b) at a wide range of pressures (0.01–10 Torr) (part (b) is reproduced from Abedini Sohi & Kahrizi [38]).

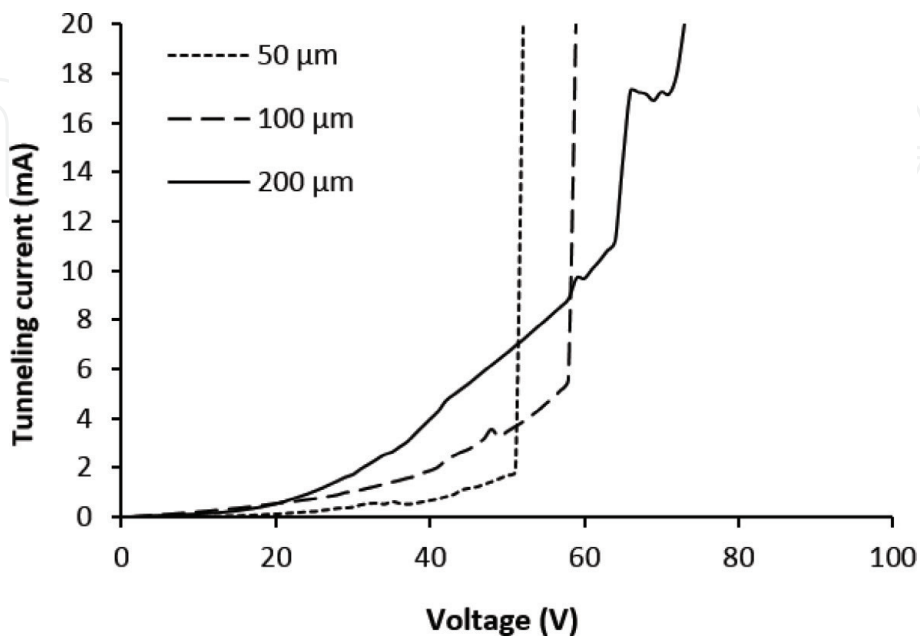


Figure 11. Fabricated GITS is tested for Ar at 10^{-2} Torr for different separation gaps. By increasing the separation gap between the electrodes, the transition from complete breakdown to quasi breakdown is observed.

7. Conclusion

A novel fabrication technique, based on consecutive chemical and electro-chemical etching techniques, is used to fabricate Si nanostructures. Si surface is textured by pyramidal hillocks through anisotropic etching in TMAH based solution. Electrochemical etching (anodic etching) of the textured Si was carried out in a HF-based solution in an electrochemical cell. Non-uniform distribution of the electric field induces different level of etching rate over the anode, which results in formation of the arrow shape structures. Mechanism of the developed structures is investigated by modeling and simulation by COMSOL multiphysics. Fabricated structures were applied as the anode in GITS. The total field enhancement coefficient (β_{tot}) of the GITS is estimated based on the ohmic region of the gas discharge characteristics, as compared to a parallel-plates sensor. Field penetration and band bending at the surface of p-type nanostructures lead to tunneling current in the range of mA in low voltages and as a result, the fabricated Si nanostructure based GITS showed the capability to distinguish the unknown gases as well as the gas pressure.

Acknowledgements

This work was partially supported by the Natural Sciences and Engineering Research Council of Canada (NSERC) and by the Gina Cody school of Engineering and Computer Science at Concordia University.

Conflict of interest

Parsou Abedini Sohi and Mojtaba Kahrizi declare that this article does not contain any conflict of interest.

IntechOpen

Author details

Parsoua Abedini Sohi and Mojtaba Kahrizi*
Concordia University, Montreal, QC, Canada

*Address all correspondence to: mojtaba.kahrizi@concordia.ca

IntechOpen

© 2019 The Author(s). Licensee IntechOpen. This chapter is distributed under the terms of the Creative Commons Attribution License (<http://creativecommons.org/licenses/by/3.0>), which permits unrestricted use, distribution, and reproduction in any medium, provided the original work is properly cited. 

References

- [1] Mandelis A, Christofides C. *Physics, Chemistry and Technology of Solid State Gas Sensor Devices*. New York: Wiley; 1993
- [2] Korotcenkov G. *Handbook of Gas Sensor Materials*. New York, Heidelberg Dordrecht London: Springer; Vol. 1 and 2; 2014
- [3] Sadeghian RB. *A Field Effect Gas Sensor Based on Self-Standing Nanowire Array*. Montreal, Canada: Concordia University; 2007
- [4] Liedberg B, Nylander C, Lunstrom I. Surface plasmon resonance for gas detection and biosensing. *Sensors and Actuators*. 1983;**4**:299-304
- [5] Sharma AK, Pandey AK, Kaur B. A review of advancements (2007-2017) in plasmonics-based optical fiber sensors. *Optical Fiber Technology*. 2018;**43**:20-34
- [6] Elosua C, Matias IR, Barriain C, Arregui FJ. Volatile organic compound optical fiber sensors: A review. *Sensors*. 2006;**6**(11):1440-1465
- [7] Gupta BD, Verma RK. Surface plasmon resonance-based fiber optic sensors: Principle, probe designs, and some applications. *Journal of Sensors*. 2009;**2009**:12
- [8] Hodgkinson J, Tatam RP. Optical gas sensing: A review. *Measurement Science and Technology*. 2013;**24**(1):1-59
- [9] Howaston AM. *An Introduction to Gas Discharges*. 2nd ed. Oxford: Pergamon Press; 1976
- [10] Liang J. Surface plasmon resonance: An introduction to a surface spectroscopy technique. *Journal of Chemical Education*. 2011;**87**(7):742-746
- [11] Homola J. *Surface Plasmon Resonance Based Sensors*. Springer; 2006
- [12] Manera MG, Rella R. Improved gas sensing performances in SPR sensors by transducers activation. *Sensors and Actuators B: Chemical*. 2013;**179**:175-186
- [13] Agbor NB, Cresswell JP, Petty MC, Monkman AP. An optical gas sensor based on polyaniline Langmuir-Blodgett films. *Sensors and Actuators B: Chemical*. 1997;**41**(1-3):137-141
- [14] Maharana PK, Jha R, Padhy P. On the electric field enhancement and performance of SPR gas sensor based on graphene for visible and near infrared. *Sensors and Actuators B: Chemical*. 2015;**207**(Part A):117-122
- [15] Nooke A et al. On the application of gold based SPR sensors for the detection of hazardous gases. *Sensors and Actuators B: Chemical*. 2010;**149**(1):194-198
- [16] Roh S, Chung T, Lee B. Overview of the characteristics of micro- and nano-structured surface plasmon resonance sensors. *Sensors*. 2011;**11**(2):1565-1588
- [17] Tosi D, Poeggel S, Iordachita I, Schena E. Fiber optic sensors for biomedical applications. In: *Opto-Mechanical Fiber Opt Sensors*. 2018. pp. 301-333
- [18] Stewart G, Tandy C, Moodie D, Morante MA, Dong F. Design of a fibre optic multi-point sensor for gas detection. *Sensors and Actuators B: Chemical*. 1998;**51**(1-3):227-232
- [19] Shemshad J. Design of a fibre optic sequential multipoint sensor for methane detection using a single tunable diode laser near 1666 nm. *Sensors and Actuators B: Chemical*. 2013;**186**:466-477
- [20] Shemshad J, Aminossadati SM, Kizil MS. A review of developments in near infrared methane detection based on tunable diode laser.

Sensors and Actuators B: Chemical.
2012;**171-172**:77-92

[21] Schwotzer G, Latka I, Lehmann H, Willsch R. Optical sensing of hydrocarbons in air or in water using UV absorption in the evanescent field of fibers. *Sensors and Actuators B*. 1997;**39**:38-39

[22] Mishra SK, Tripathi SN, Choudhary V, Gupta BD. SPR based fibre optic ammonia gas sensor utilizing nanocomposite film of PMMA/reduced graphene oxide prepared by in situ polymerization. *Sensors and Actuators B: Chemical*. 2014;**199**:190-200

[23] Hall F, Hill B. *Plasma Gas Disch*, Vol. 92000. pp. 1-11

[24] Boyle WS, Kisliuk P. Departure from Paschen's law of breakdown in gases. *Physics Review*. 1955;**97**(2):255-259

[25] Lisovskii VA, Yakovin SD. A modified Paschen law for the initiation of a dc glow discharge in inert gases. *Technical Physics*. 2000;**45**(6):727-731

[26] Radmilović-Radjenović M, Radjenović B. An analytical relation describing the dramatic reduction of the breakdown voltage for the microgap devices. *Europhysics Letters*. 2008;**83**(2):25001

[27] Chivu N, Kahrizi M. Design, Modeling and Simulation of a Miniaturized Gas Ionization Sensor: Optimization of the Structure and Operation; 2012. pp. 178-183

[28] Chivu N, Kahrizi M. Modeling and simulation of a miniaturized gas ionization sensor: Detection of greenhouse gases. *Sensors & Transducers*. 2013;**153**(6):105-110

[29] Jensen KL, Shiffler DA, Harris JR, Rittersdorf IM, Petillo JJ. 2D/3D image charge for modeling field emission. *Journal of Vacuum Science & Technology, B: Nanotechnology &*

Microelectronics: Materials, Processing, Measurement, & Phenomena. 2017;**35**(2):02C101

[30] Yilmazoglu O et al. Electron field emission from nanostructured semiconductors under photo illumination. *Turkish Journal of Physics*. 2014;**38**(3):543-562

[31] Saito Y, Uemura S. Field emission from carbon nanotubes and its application to electron sources. *Carbon*. 2000;**38**(2):169-182

[32] Modi A, Koratkar N, Lass E, Wei B, Ajayan PM. Miniaturized gas ionization sensors using carbon nanotubes. *Nature*. 2003;**424**:171-174

[33] Yeow JTW, Wang Y. A review of carbon nanotubes-based gas sensors. *Journal of Sensors*. 2009;**2009**:24

[34] Kim SJ. Gas sensors based on Paschen's law using carbon nanotubes as electron emitters. *Journal of Physics D: Applied Physics*. 2006;**39**(14):3026-3029

[35] Sadeghian RB, Kahrizi M. A novel miniature gas ionization sensor based on freestanding gold nanowires. *Sensors and Actuators, A: Physical*. 2007;**137**(2):248-255

[36] Azmoodeh N, Chivu N, Sadeghian RB, Kahrizi M. A silver nanowire based gas ionization sensor EUROCON 2009. In: *IEEE EUROCON 2009*. 2009. pp. 1231-1235

[37] Sadeghian RB, Kahrizi M. A novel gas sensor based on tunneling-field-ionization on whisker-covered gold nanowires. *IEEE Sensors Journal*. 2008;**8**(2):161-169

[38] Abedini Sohi P, Kahrizi M. Low-voltage gas field ionization tunneling sensor using silicon nanostructures. *IEEE Sensors Journal*. 2018;**18**(15):6092-6096

[39] Edgcombe CJ, Valdrè U. Microscopy and computational modelling to elucidate the enhancement factor for field electron emitters. *Journal of Microscopy*. 2001;**203**(2):188-194

[40] Forbes RG, Edgcombe CJ, Valdrè U. Some comments on models for field enhancement. *Ultramicroscopy*. 2003;**95**:57-65

[41] Zou R, He G, Xu K, Liu Q, Zhang Z, Hu J. ZnO nanorods on reduced graphene sheets with excellent field emission, gas sensor and photocatalytic properties. *Journal of Materials Chemistry A*. 2013;**1**(29):8445-8452

[42] Charlier JC et al. Enhanced electron field emission in B-doped carbon nanotubes. *Nano Letters*. 2002;**2**(11):1191-1195

[43] Sohi PA, Kahrizi M. Formation mechanism of silicon nanowires using chemical/electrochemical process. *IEEE Transactions on Nanotechnology*. 2017;**16**(3):507-513

IntechOpen